

Assessment of noise in InSAR timeseries using least squares variance component estimation

Sasan Babae¹, Masoud Mashhadi Hossainali^{*1}, Sami Samie Esfahany²

⁽¹⁾ Department of Geodesy and Geomatics Engineering, K. N. Toosi University of Technology, Tehran, Iran

⁽²⁾ School of Surveying and Geospatial Engineering, College of Engineering, University of Tehran, Iran

Article history: received November 25, 2021; accepted March 24, 2022

Abstract

In recent decades, Interferometric Synthetic Aperture Radar (InSAR) has progressed as an effective and reliable tool for monitoring the surface deformations of the earth. Despite the potential of this method for deformation monitoring, the quality description of InSAR timeseries in terms of precision and noise structure and, consequently, the precision of the InSAR-derived parameters (e.g., displacement and its velocity) are still somewhat ambiguous. In this paper, we propose to estimate the precision and noise structure of the final InSAR products in a well-established methodology called multivariate Least Squares Variance Component Estimation (LS-VCE). The advantage of this methodology is its capability to simultaneously account for both spatial and temporal noise structures in spatiotemporally correlated data such as InSAR timeseries. Although this methodology has been already used extensively for GNSS data, its application on InSAR data has been limited to very simplified scenarios. Also, due to the large data volume and the ambiguities in the InSAR noise structure estimation, the application of LS-VCE requires some algorithm modification/adaptation. Here, to demonstrate the applicability of the proposed framework, we applied it on the deformation timeseries derived from the Sentinel-1 data over the city of Tehran, Iran. The results show that applying the multivariate LS-VCE method in our case study improves the velocity-rate precision by about 50% compared with the case where the noise parameters are not considered. In addition, the results confirm the fact that InSAR timeseries are highly correlated in time and space. It should be noted that the observed spatial correlation should be differentiated from the well-known spatial correlation imposed by atmospheric components. In fact, due to the atmosphere filtering step, the noise structure of the final results would be different from the statistical characteristics of a raw atmospheric signal. The proposed methodology is not case study dependent and can be used as an appropriate approach to provide the precision (as a quality descriptor) of the timeseries InSAR products.

Keywords: Radar Interferometry; InSAR; Least Squares Variance Component Estimation (LS-VCE); Spatio-Temporal Correlation; Covariance Matrix

1. Introduction

Monitoring and analysis of gradual surface displacements are key factors in recognition of the behaviour of the earth's deformation. Multi-temporal SAR interferometric timeseries methods use a multitude of satellite radar images to estimate the spatio-temporal evolution of surface deformation [Hanssen 2001; Berardino et al. 2002; Lanari et al. 2004]. An important issue regarding the InSAR-derived displacement timeseries is their noise structure [Hanssen, 2001; González and Fernandez, 2011]. The noise in SAR timeseries should be analysed to obtain an accurate assessment of the model parameters, describing the earth displacement, e.g., the site velocity. The importance of this issue is also revealed when one encounters the estimation of the precision of the InSAR-derived geo-model parameters, e.g., earthquake and volcano source parameters.

A challenging aspect of quality description of final InSAR timeseries is that the initial noise structure of data are affected and modified by various spatial or temporal filtering steps applied in timeseries InSAR algorithms. In other words, the spatio-temporal filtering steps, which effectively mitigate the decorrelation and atmospheric noise, alters the initial spatio-temporal characteristics of these noise components. Therefore the common and well-studied stochastic models of initial noise components (e.g., pure atmospheric signal or decorrelation noise) cannot accurately describe the precision of final/processed InSAR timeseries. Also, it should be noted that, as the filtering step and its setting vary from case to case, it is challenging to derive a generic analytical formulation for the precision and quality description of InSAR deformation timeseries.

To provide the noise structure of InSAR timeseries (either before or after filtering steps), many efforts have been made for modelling the noise components and their statistical properties [Davenport and Root, 1958; Lucido et al., 2009; Dainty, 2013; Samiei Esfahany, 2017]. For example, one of the first studies conducted by Hanssen [2001] introduced a mathematical framework to evaluate the fundamental source of errors in each interferogram based on the coherence factor and the spatial analysis of atmospheric variability. Later, Guarnieri and Tebaldini [2007] proposed a hybrid Cramer-Rao bound for the InSAR-based deformation estimates based on a coherence matrix and a simple atmospheric disturbance model. González and Fernandez [2011] presented a method based on spatio-temporal correlation in interferograms accompanied by the Monte Carlo manner for calculating interferograms covariance matrices and propagate them to unknown displacement parameters. Agram and Simons [2015] have developed a simple multi-interferograms error propagation to estimate a full spatio-temporal noise covariance matrix using a network of interferograms. Samiei-Esfahany and Hanssen [2017] presented a general closed-form equation for the interferometric phase covariance based on the nonlinear error propagation of SAR statistics and only for decorrelation effects. We can also refer to Cao et al. [2018], that proposed a methodology to construct the covariance matrix of atmospheric signal in InSAR timeseries.

Despite the previous studies to evaluate and assess the noise variability and its structure in raw InSAR timeseries (i.e., before spatio-temporal filtering) [Hanssen, 2001; Guarnieri and Tebaldini, 2007; González and Fernandez, 2011; Mehrabi et al., 2019], the noise assessment of final InSAR timeseries has been remarkably overlooked so far. Most of the works mentioned above provide an estimate of the interferogram noise model and investigate its impact on the formation of the timeseries. However, the issue of error propagation (from the raw timeseries to the final filtered timeseries) has received less attention due to the complexity of the processing steps, incomplete information on the initial noise structures, and a non-comparative strategy of filtering among different software tools and algorithms. So, it is desirable to have a generic quality description approach that is independent of the applied processing algorithm.

In this paper, we presented a data-derived approach to estimate the precision of the final InSAR deformation timeseries, using multivariate Least Squares Variance Component Estimation (LS-VCE). The value of multivariate LS-VCE has been well recognized in noise analysis of geodetic data such as GNSS timeseries [Amiri-Simkooei 2009], Buoy tide measurements and satellite altimetry data [Farzaneh et al. 2020] but is limited in the InSAR data. Some examples of its application in InSAR literature have been presented by Kampes (2006), Ketelaar (2009), and Van Leijen (2014), who have adopted some practical and simplified scenarios to apply LS-VCE on InSAR data. The limitations of these studies can be mentioned as: (i) using pre-assumed noise structures that are not based on identifying the appropriate noise structure in the data (ii) the LS-VCE was carried out in either time or space domain (or in a disjoint manner).

The LS-VCE method has some advantages, such as the capability to account for spatial-temporal noise structures and compatibility with digesting various sources of user-controlled stochastic noise structures. Indeed, Unlike the univariate LS-VCE noise assessment method [Amiri-Simkooei 2007; Amiri-Simkooei, Tiberius, and Teunis-

sen 2007], this method allows the simultaneous estimation of spatio-temporal noise components and provides the possibility of constructing a multi-variable noise structure or noise covariance matrix.

The objective of this study is to directly estimate the noise components of the final InSAR timeseries by offering the data-driven precision descriptor based on the multivariate LS-VCE method. It should be noted that the proposed method is flexible to digest different combinations of noise components, while the optimal combination is then selected based on a maximum likelihood approach. In this particular study, considering the previous experiences of noise modelling in geodetic data, a composition of flicker, white, and first-order autoregressive noises is used for generating cofactor matrices in the noise model. The proposed approach is applied and demonstrated over the case study of Tehran, Iran. After applying the multivariate LS-VCE method on InSAR-derived timeseries and extracting noise variance components, we validate the proposed approach results using available GPS data.

The paper is continued as follows: Section 2 goes over the main methods for the InSAR timeseries analysis and the spatio-temporal noise problem. Section 3 explains the basic concepts of multivariate LS-VCE. We describe our proposed noise assessment model in the InSAR timeseries in section 4, along with the details of implementation steps and the whole work algorithm. In section 5, we apply the new noise estimation method on the InSAR timeseries in Tehran along with the derived primary results. Finally, Sections 6 and 7 present the validation and comparison of the final results with GPS data and conclusions, respectively.

2. InSAR Timeseries

The essential concept of Timeseries InSAR (TInSAR) methodologies is firstly to unwrap the wrapped InSAR timeseries, and secondly to isolate desired displacement signals from noise or other disturbing signals. TInSAR methods are based on the systematic production of multiple interferograms from an area of interest (AOI) during a period of time. Several TInSAR algorithms are available to process the interferograms and extract the deformation timeseries.

The first efforts of TInSAR analysis were known as stacking [Sandwell and Price, 1998; Strozzi et al., 2001], which reduced atmospheric effects by a temporal averaging over a series of interferograms. Concentration on identifying coherent pixels, which are least influenced by decorrelation noise in interferograms, provides the foundation for developing other TInSAR methods called persistent scatterer InSAR (PSInSAR) [Ferretti, Prati, and Rocca, 2001]. The same idea became the basis for other compatible methods, collectively named persistent scatterer interferometry (PSI) [Adam, Worawattanamateekul, and Kircher, 2004; Van der Kooij, 2003; Hooper et al., 2004; Kampes, 2006; Costantini et al. 2009; Van Leijen 2014]. Parallel with the PSI methods, another set of techniques aimed at extracting coherent pixels in interferograms with small perpendicular and temporal baselines [Berardino et al. 2002]. Nevertheless, these two groups complementing each other lead to the invention of another set of methods, called hybrid methods, such as the merging method exploited in StaMPS/MTI and SqueeSAR [Lanari et al., 2004; Hooper, 2006].

The common goal of all the timeseries analysis methods mentioned above is to provide a reliable displacement timeseries for each point with an emphasis on minimizing the noise in these series. However, even applying the most precise TInSAR methods, some parts of noise have still remained in output results, often causing oscillations or perturbations in the timeseries at any point. It is well known that the multiple uses of a common SAR image to form several interferograms in TInSAR algorithms introduce a correlation among noise components of the constructed interferograms [González and Fernandez, 2011], making the observations and their noise characteristics dependent in the time domain (temporal correlation). Further, an overlap between baseline spectrum or temporal interval of interferograms, a correlation between SAR acquisitions (manifested in coherence between them), and also use of inversion processes (e.g., least squares inversion, phase triangulation) can produce a temporal correlation between interferograms [Agram and Simons, 2015; Samiei Esfahany, 2017]. On the other hand, other sources of errors, such as Atmosphere Phase Screen (APS), imposed spatially correlated noise structure in the data [Hanssen, 2001]. Moreover, spatio-temporal filtering steps applied to InSAR timeseries (e.g., multi-looking, atmosphere filtering, etc.) can introduce spatial and temporal correlation in the results. The spatio-temporal correlation between PS-pixels and also between interferograms is a critical issue that should be accounted for in the quality description of TInSAR products. Ignoring this correlation may lead to an under-/over-estimation of the precision of the final filtered timeseries and their derived products. This paper attempts to investigate the existence of this correlation in timeseries and propose a methodology to extract the stochastic model of final TInSAR in an objec-

tive manner. The proposed framework is based on multivariate LS-VCE, which will be discussed in more details in the next section.

3. Multivariate LS-VCE

Several methods can conduct an assessment of the noise characteristics of the geodetic timeseries. In this regard, we can mention the Maximum Likelihoods Estimation (MLE), Least Square Estimation (LSE), Bayes Parameter Estimation (BPE), and different existing VCE methods, such as Best Invariant Quadratic Unbiased Estimation (BIQUE), Minimum norm Quadratic Unbiased Estimator (MINQUE), Restricted Maximum Likelihood (REML) and so on [Crocetto, Gatti, and Russo, 2000; Wang, Satirapod, and Rizos 2002; Amiri-Simkooei and Tiberius 2004; Zhang et al. 2004; Kubik 1970; Rao 1971; Koch 1986]. Among the VCE methods, the LS-VCE has several attractive and unique properties such as unbiasedness and minimum variance property and the flexibility to apply hypothesis testing to the stochastic model [Amiri-Simkooei, et al., 2007; Amiri-Simkooei, 2009]. Furthermore, it can be shown that in the particular case of Gaussian noise structures, the LS-VCE is equivalent to other VCE methods [Amiri-Simkooei, Tiberius, and Teunissen 2007]. In general, the LS-VCE approach is easily adapted to cope with any type of noise in the data and directly provides covariance estimators' precision [Amiri-Simkooei, 2009].

Teunissen and Amiri-Simkooei [2008] developed and applied the LS-VCE method to assess the noise characteristics of geodetic timeseries and, in particular, GPS data. In this method, the mathematical model of the problem can be divided into two parts: i) the functional model that describes the relationship between the observations and the unknown parameters and ii) the stochastic model that characterises a priori precision of the observations through its covariance matrix. The univariate LS-VCE model with p categories of noise structure in the timeseries data can be written as:

$$\begin{cases} E(\underline{y}) = Ax \\ D(\underline{y}) = Q_y = Q_0 + \sum_{k=1}^p \sigma_k Q_k \end{cases} \quad (1)$$

Where \underline{y} represents the vector of observables, x is the vector of estimated parameters, and A is a design matrix with full column rank relating the observations in \underline{y} to the unknown parameters in x and also E , D are the expectation and dispersion operators, respectively. The Q_y covariance matrix corresponding to observations is expressed as a linear combination of p -number known cofactor matrices Q_k with the scale of unknown variance components σ_k plus Q_0 as a known part of the cofactor matrix of the stochastic model (if it exists). Each cofactor matrices describes the noise structure of different sources.

The cofactor matrices Q_k are assumed to be symmetric and linearly independent as necessary conditions for the stochastic model to have a regular solution [Amiri-Simkooei, Tiberius, and Teunissen, 2007]. The univariate LS-VCE model can estimate the variance components under an iterative procedure. It estimates parameters from each timeseries independent of others and neglects the correlation between different timeseries.

Williams et al. [2004] showed the possibility of spatially correlated noise components in geodetic observations and demonstrates that it is not realistic to analyse timeseries individually and neglects the spatial correlation between them. Therefore, the simultaneous and multivariate analysis would be preferred instead of univariate analysis. If we consider both temporal and spatial correlated components, then the LS-VCE method enables us to estimate all parameters simultaneously. Amiri-Simkooei [2009] suggested that a sophisticated strategy includes both the temporal and spatial correlation, called the multivariate LS-VCE method (Figure 1). Considering r -timeseries data and substituting the assembled form of $X = (x_1, \dots, x_r)$ (unknown vectors), $\underline{Y} = (\underline{y}_1, \dots, \underline{y}_r)$ (observable vectors), and $\underline{E} = (\underline{e}_1, \dots, \underline{e}_r)$ (residual vectors) in Eq. (1), the linear model of the observation-equations of this method is written as

$$\begin{cases} E(\text{vec}(\underline{Y})) = (I_r \otimes A)\text{vec}(X) \\ D(\text{vec}(\underline{Y})) = \Sigma \otimes \left(\sum_{k=1}^p \sigma_k Q_k \right) \end{cases} \quad (2)$$

In the above compact notation, the symbols $\text{vec}(\cdot)$ and \otimes represent the operator of Vec and the Kronecker product, respectively. Note that the matrix Σ is unknown and is called the cross (spatial)-correlation matrix between timeseries (see, Eq. (15)). We can now apply the multivariate LS-VCE manner to simultaneous estimation of both X and Σ by the iteration algorithmic process presented in Figure 1 (for more details, see Appendix). In the next section, we describe the flowchart implementation steps of the proposed method in this paper.

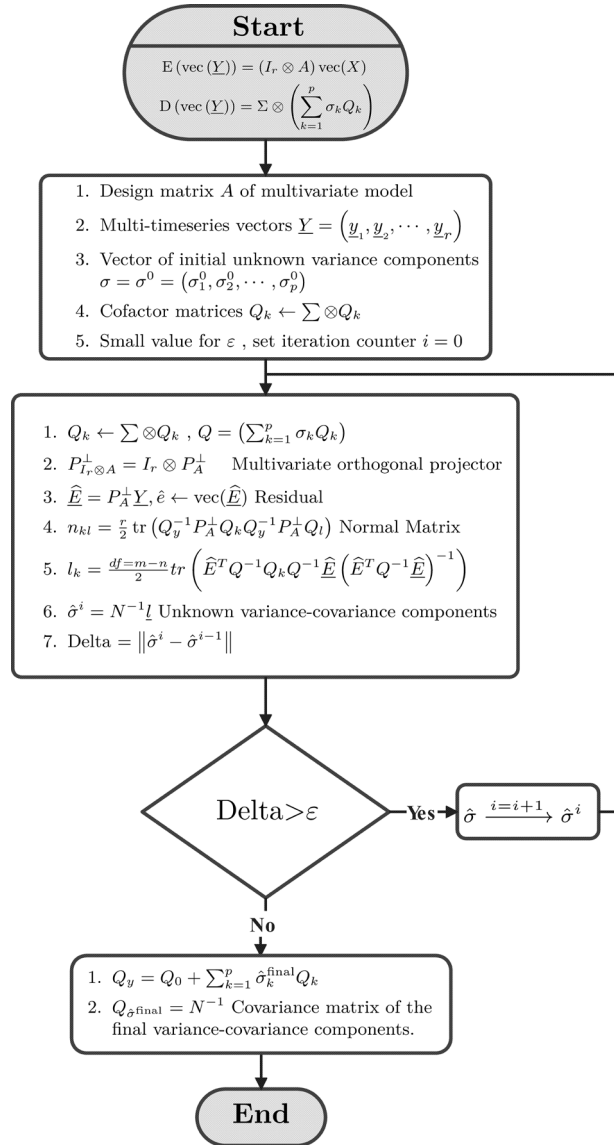


Figure 1. Flowchart of the algorithm used to implement multivariate LS-VCE, see more details in [Amiri-Simkooei, Teunissen, and Teunissen 2007; Amiri-Simkooei 2009].

4. Methodology

This paper has considered the stochastic model as a more practical model, according to the categories of stochastic models presented in [Amiri-Simkooei, 2009], to evaluate the timeseries noise components of PSs by using the multivariate LS-VCE. The reason for choosing this model is that the relative amplitudes of various noise components are generally unknown. We employed different PSs timeseries together located inside a spatial class to calculate estimated parameters (i.e., site velocities) and their precision. Figure 2 illustrates the flowchart of multi-temporal InSAR timeseries processing and its noise assessment error in the LS-VCE framework.

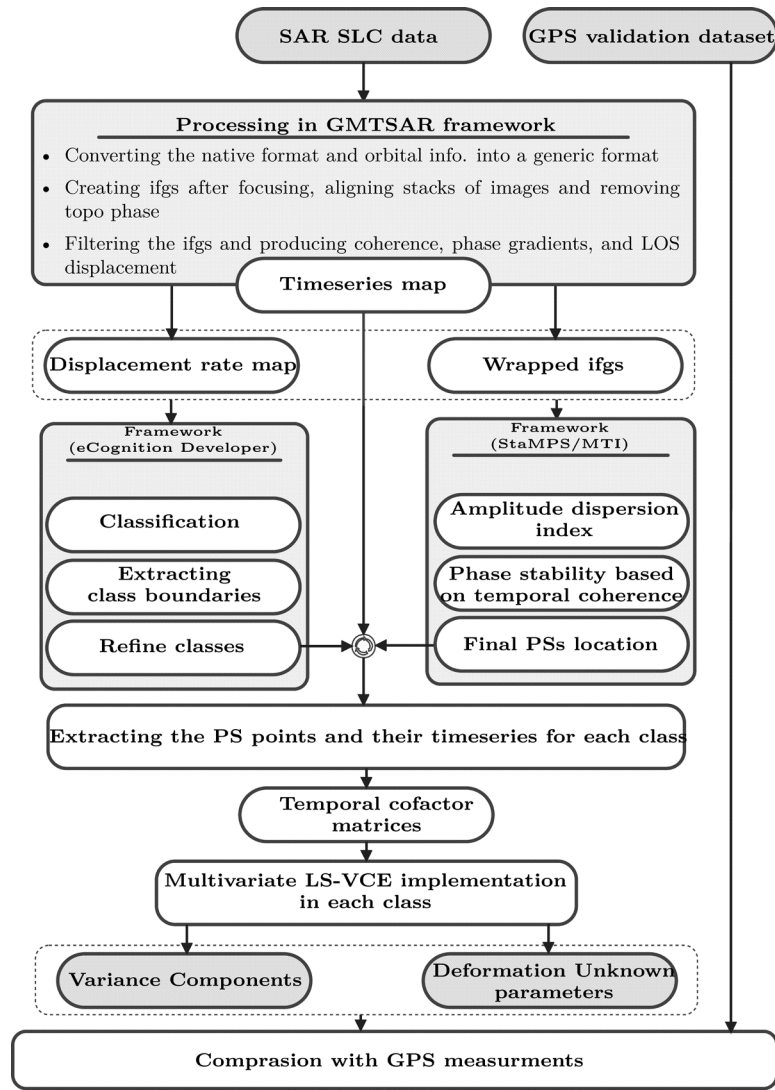


Figure 2. Schematic program flowchart of multi-temporal InSAR timeseries processing and its noise assessment error with multivariate LS-VCE method (see the text box for details). Note that the abbreviations info., ifgs, defo and topo refer to information, interferograms, deformation, and topographic, respectively.

4.1 Processing Steps

Initially, a series of radar images (N number of SLC images) are processed based on a coherence-based SBAS timeseries approach. This set of SAR images are used to produce field deformation rates with GMTSAR software [Sandwell et al., 2011] operating based on the three main components (See the first block of Figure 2). The final output of the first block, including displacement rate map, displacement timeseries, and wrapped interferograms, are extracted for classification, noise analysis, and PS-pixels identification, respectively.

Hence, for identifying PS pixels based on amplitude dispersion index (ADI) and temporal coherence [Hooper, 2006; Hooper and Zebker, 2007], we apply the Stanford method of InSAR analysis, called StaMPS [Hooper, 2006]. The details of the processing in StaMPS are well documented in [Hooper, 2006; Hooper and Zebker, 2007] articles. Also, in order to apply the multivariate LS-VCE, we need to classify the detected PSs with similar temporal behaviour. Cross correlations, the spatial correlation, are given by the matrix Σ , which is the size of $r \times r$. This matrix and the time correlation of the timeseries (e.g., components σ_k) can be estimated by Eq. (8). As inferred from this equation, the total matrix Σ of the whole AOI has a full structure, which could be on the order of a few million components. Therefore, if one includes more timeseries in the model, the computational load will be increased significant. Furthermore, estimating the covariance matrix of the model parameters from Eq. (12) involves the computation of the matrix Σ , rendering it computationally intractable on conventional computers. Therefore, to

avoid large matrices and reduce the inherent computational complexity of the VCE process, we divide the study area into smaller segments based on the spatial pattern in the displacement rate map.

Note that the classification here is applied only to reduce the computational load of the VCE process, and the variance components are estimated finally for each individual PS. Therefore the choice for the classification criterion is arbitrary and does not have any effect on the final results. We use eCognition Developer software to segmentation/classify the final displacement rate map [Batz et al., 2004]. After segmentation/classification, we extract the PSs points with similar spatio-temporal timeseries for each class based on the StaMPS Framework, and classes that do not include any PSs are removed from our noise processing (refining classes).

4.2 Noise Models

In the following, we use the multivariate LS-VCE analysis for each class to calculate the noise components' amplitude in the timeseries of classified PSs. In this step, to construct the cofactor matrices for InSAR data, we have considered a combination of flicker, white, and first-order autoregressive AR(1) noises. As mentioned earlier, there is no clear noise model to describe the noise structure in InSAR timeseries. However, based on the most common noise sources in geodetic data (and in particular InSAR timeseries), we consider three noise structures in this study, as follows.

- 1) **White noise:** the reasons for the existence of this noise model are the PS decorrelation phase and residual atmospheric noise [Sudhaus and Sigurjón 2009] and q_{PS}^w (unit: mm^2) the elements of the white noise cofactor matrix Q_w for each PS point timeseries can be written as

$$\tau = |t_k - t_l|, \quad q_{PS}^w = \begin{cases} 1 & (\text{if } \tau = 0) \\ 0 & (\text{if } \tau \neq 0) \end{cases} \quad (3)$$

where the τ is the absolute magnitude of the time difference between the two observation epochs k and l .

- 2) **The first-order autoregressive AR(1) noise:** this component may be induced by a deviation of deformation from the assumed functional model and can also be induced by low pass filters applied in the processing chain [Samiei Esfahany, 2017]. The first-order autoregressive noise cofactor matrix Q_a elements q_{PS}^a (unit: mm^2) are given as [Amiri-Simkooei, Tiberius, and Teunissen 2007]:

$$\tau = |t_k - t_l|, \quad q_{PS}^a = \begin{cases} 1 & (\text{if } \tau = 0) \\ e^{-\alpha\tau} & (\text{if } \tau \neq 0) \end{cases} \quad (4)$$

In the autoregressive noise equation, a time-scale parameter α shows the temporal correlation rate of the signal. This parameter was derived using InSAR data through the w -test statistic, with the most probable value of ~ 0.05 . In fact, for autoregressive noise, we calculate the w -test statistic for different values of α . We then choose the α which the absolute value of the below w -test statistic was maximized [Amiri-Simkooei 2007].

$$\underline{w} = \frac{b \operatorname{tr}(\hat{\underline{E}}^T Q_a \hat{\underline{E}} \Sigma^{-1}) - r \operatorname{tr}(Q_a P_A^\perp) \operatorname{tr}(\hat{\underline{E}}^T \hat{\underline{E}} \Sigma^{-1})}{[2b^2 r \operatorname{tr}(Q_a P_A^\perp Q_a P_A^\perp) - 2r^2 b \operatorname{tr}(Q_a P_A^\perp) \operatorname{tr}(Q_a P_A^\perp)]^{1/2}} \quad (5)$$

Where Q_a is the autoregressive cofactor matrix for different α values and also $b = (m - n)r$ is the degree of freedom that m , n , and r parameters are the number of observations, the number of unknowns, and the number of timeseries, respectively.

- 3) **Flicker noise:** This component is induced by electronic devices and their characteristics [Van der Ziel 1979]. Although this kind of noise is most common in GPS datasets, but as radar is an electronic device, we consider

it as a potential noise model also for the InSAR timeseries also Bui [2021] recommends that this noise model be considered in the InSAR timeseries analysis and error estimation. The flicker noise cofactor matrix Q_f can be constructed as [Zhang et al., 1997].

$$\tau = |t_k - t_l|, \quad q_{PS}^f = \begin{cases} \frac{9}{8} & (\text{if } \tau = 0) \\ \frac{9}{8} \left(1 - \frac{\log \tau / \log 2 + 2}{24} \right) & (\text{if } \tau \neq 0) \end{cases} \quad (6)$$

Note that the proposed methodology is flexible to digest other noise sources also. Again, the reason for applying the introduced noise models is that they are a more generic case and have been used widely in geodetic timeseries. After defining the noise structures, we can decide which combination of these models is the most likely optimal combination by the maximum likelihood method as described in the next section.

4.3 Noise Models Selection

After applying the iterative multivariate LS-VCE algorithm using different noise models, the maximum likelihood estimation (MLE) is used to determine the observations' appropriate noise structure. Using this method made it possible to decide which type of noise structure (temporal cofactor) should be included in the stochastic model. According to this method, the observables have a multivariate normal distribution as $\underline{y} \sim N(Ax, \sum_{k=1}^p \sigma_k Q_k)$; accordingly, we should maximize the likelihood function for the multivariate stochastic model to maximize the probability distribution function of observations described by [Amiri-Simkooei, Tiberius, and Teunissen 2007].

$$\ln L(\underline{y}; x, \sigma) = -\frac{mr}{2} \ln 2\pi - \frac{1}{2} \{m \ln \det(\Sigma) + r \ln \det(Q)\} - \frac{r(m-n)}{2} \quad (7)$$

Here \ln is the natural logarithm. The results of using this method to turn out the appropriate noise model are discussed in section 6 (subsection headed "LS-VCE per class").

4.4 Estimating the multivariate noise structure

Next to the appropriate noise model selected, the estimate of the unknown matrix $\underline{\hat{\Sigma}}$ is obtained as follows:

$$\underline{\hat{\Sigma}} = \frac{\hat{\underline{E}}^T Q^{-1} \hat{\underline{E}}}{(m-n)}, \quad \hat{\underline{E}} = P_A^+ \underline{Y} = (\hat{\underline{e}}_1, \hat{\underline{e}}_2, \dots, \hat{\underline{e}}_r) \quad (8)$$

Where P_A^+ is the multivariate orthogonal projector. The estimated correlation coefficient between the different PS timeseries ($\rho_{PS_{ij}}$) is obtained by $\underline{\hat{\Sigma}}$ matrix elements.

$$\rho_{PS_{ij}} = \frac{\hat{\sigma}_{PS_{ij}}}{\sqrt{\hat{\sigma}_{PS_{ii}} \hat{\sigma}_{PS_{jj}}}} = \frac{\hat{\sigma}_{PS_{ij}}}{\hat{\sigma}_{PS_i} \hat{\sigma}_{PS_j}}, \quad i, j = \{1, 2, \dots, r\} \in \text{class}_x \quad (9)$$

As you can see, the estimated correlation coefficient is a nonlinear function of the $\hat{\sigma}_{PS_i} \hat{\sigma}_{PS_j}$, and $\hat{\sigma}_{PS_{ij}}$. To get the variance of the estimated correlation coefficient, we used Eq. (10), which apply the error propagation law to the linearized form of the covariance matrix between PS timeseries i and j , and simplifies by [Amiri-Simkooei, 2009]

$$\sigma_{\rho_{PS_{ij}}}^2 = \frac{(1 - \rho_{PS_{ij}}^2)^2}{m-n}, \quad i, j = \{1, 2, \dots, r\} \in \text{class}_x \quad (10)$$

We also extracted the standard deviation $\hat{\sigma}_{PS_i}$ and its precision $\sigma_{\hat{\sigma}_{PS_i}}$ for each PS timeseries with the following relationships.

$$\hat{\sigma}_{PS_i} = \sqrt{\hat{\sigma}_{PS_i}^2} = \sqrt{\hat{\sigma}_{PS_{ii}}}, \quad \sigma_{\hat{\sigma}_{PS_i}} \approx \frac{\sigma_{\hat{\sigma}_{PS_i}^2}}{2\hat{\sigma}_{PS_i}} = \frac{\sigma_{\hat{\sigma}_{PS_{ii}}}}{2\hat{\sigma}_{PS_i}} \quad (11)$$

According to the results obtained, we can estimate the covariance matrix of the model parameters as,

$$Q_{\hat{x}} = \underline{\underline{\Sigma}} \otimes (A^T Q_y^{-1} A) \quad (12)$$

The diagonal elements of the matrix $Q_{\hat{x}}$ indicate the precision of the model parameters. In the absence of estimating the proper noise structure due to the correlation between PSs timeseries, the matrix $\underline{\underline{\Sigma}}$ is an identity matrix of size r , in which case an unrealistic estimate of the precision of the model parameters is obtained.

4.5 Validation and Comparison with GPS data

Finally, the results obtained by using the above methodology will be compared to the GPS dataset. The locations of the available GPS stations in our case study area are indicated in Figure 5.b (stations whose timeseries are available) and Figure 10.b (stations with only displacement rates are available). Note that, in order to be able to compare the InSAR-derive results and GPS data, both datasets should have the same datum (i.e., have the same reference point). We have compared the InSAR and GPS datasets using the same reference point shown by a red star in Figure 5.b.

5. Case study area, SAR data, and processing setting

The case study is the Tehran plain located in the north of Iran and the southern slopes of the Alborz mountain range (Figure 3). The studied area is of particular importance in terms of a geological structure due to the presence of two regions seriously involved in the subsidence phenomenon [Sharifi et al., 2008; Haghighi and Motagh, 2019]. These two regions include the western Tehran plain (reaching the cities of Yaftabad, Shahriyar, and Malard to the north, Tehran to the northeast, and Eslamshahr to the south) and Hashtgerd plain (including Karaj, Hashtgerd, and Najmabad cities).

We used a set of 34 C-band (~5.6 cm wavelength) Sentinel-1A SAR images collected between November 2016 and January 2018. The dataset is in the Single Look Complex (SLC) format and is acquired in interferometric wide (IW) mode with a swath width of about 250 km from ascending track number 28. The sub-swath (IW2), which fully covered our study area, has been selected for TInSAR process (as shown in Figure 3). The acquisition dates and platform characterized for SAR imagery are described in Table 1.

Sensor	Number of Images	Timeseries Period	Track	Incidence Angle (deg.)	Polarization	Mode
Sentinel-1A	34	20161113-20180131	Ascending	39.46	VV	SLC, IW

Table 1. Details of the SAR acquisitions used for the InSAR timeseries analysis.

Subsequently, we generated 84 interferograms with perpendicular and temporal baselines smaller than 50 meters and 3 months, respectively (Figure 4).

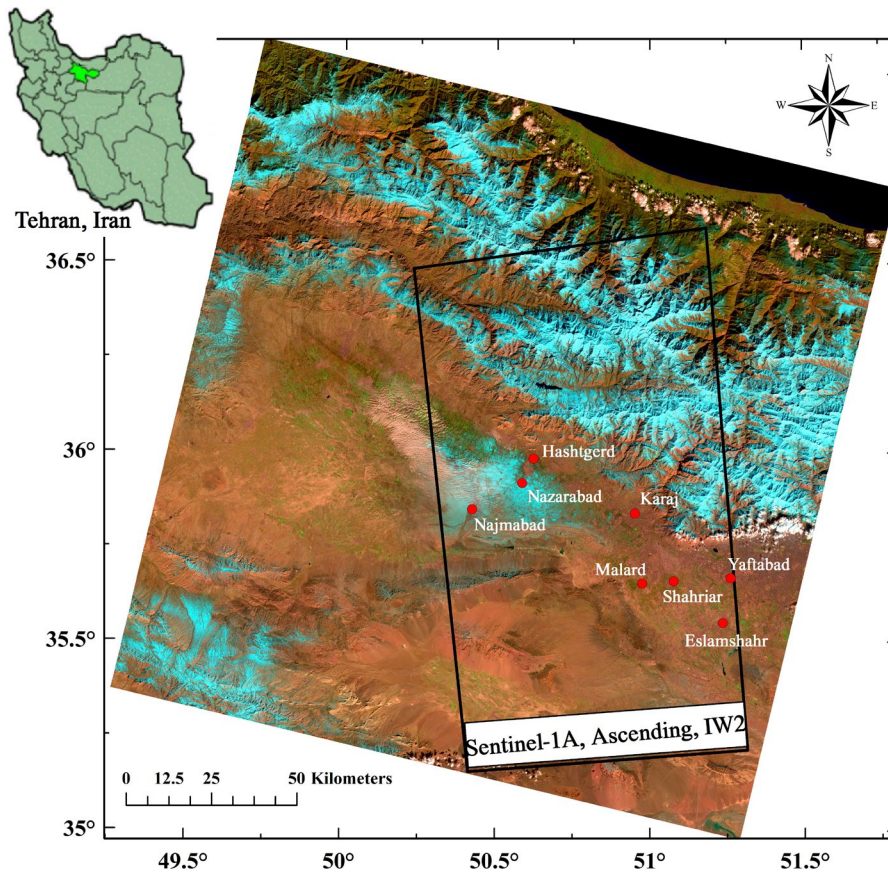


Figure 3. Landsat 8 image of the study area. The inset at the top-left indicates the location of Tehran plain in Iran. The black frame shows the swath IW2 of Sentinel-1A ascending data used in this study.

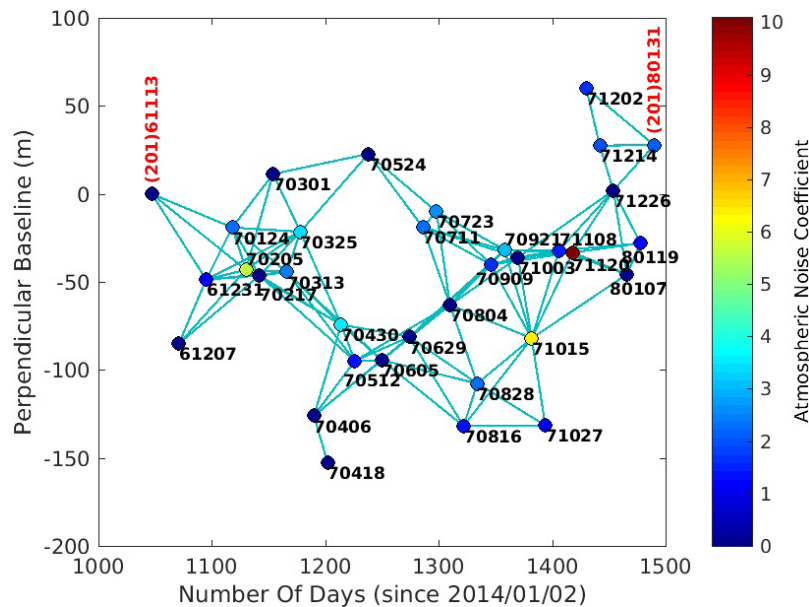


Figure 4. The final network of the selected interferograms was used for the SBAS timeseries analysis. Circles represent the images, and light-green lines indicate interferograms used in our study, and the colours of the dots indicate the atmospheric noise coefficient. The horizontal axis shows the number of days with respect to the reference date, 2 January 2014 (year of Sentinel-1A launch). The ID of the images shows their time format; for example, yyyyymmdd is shown as yymmdd.

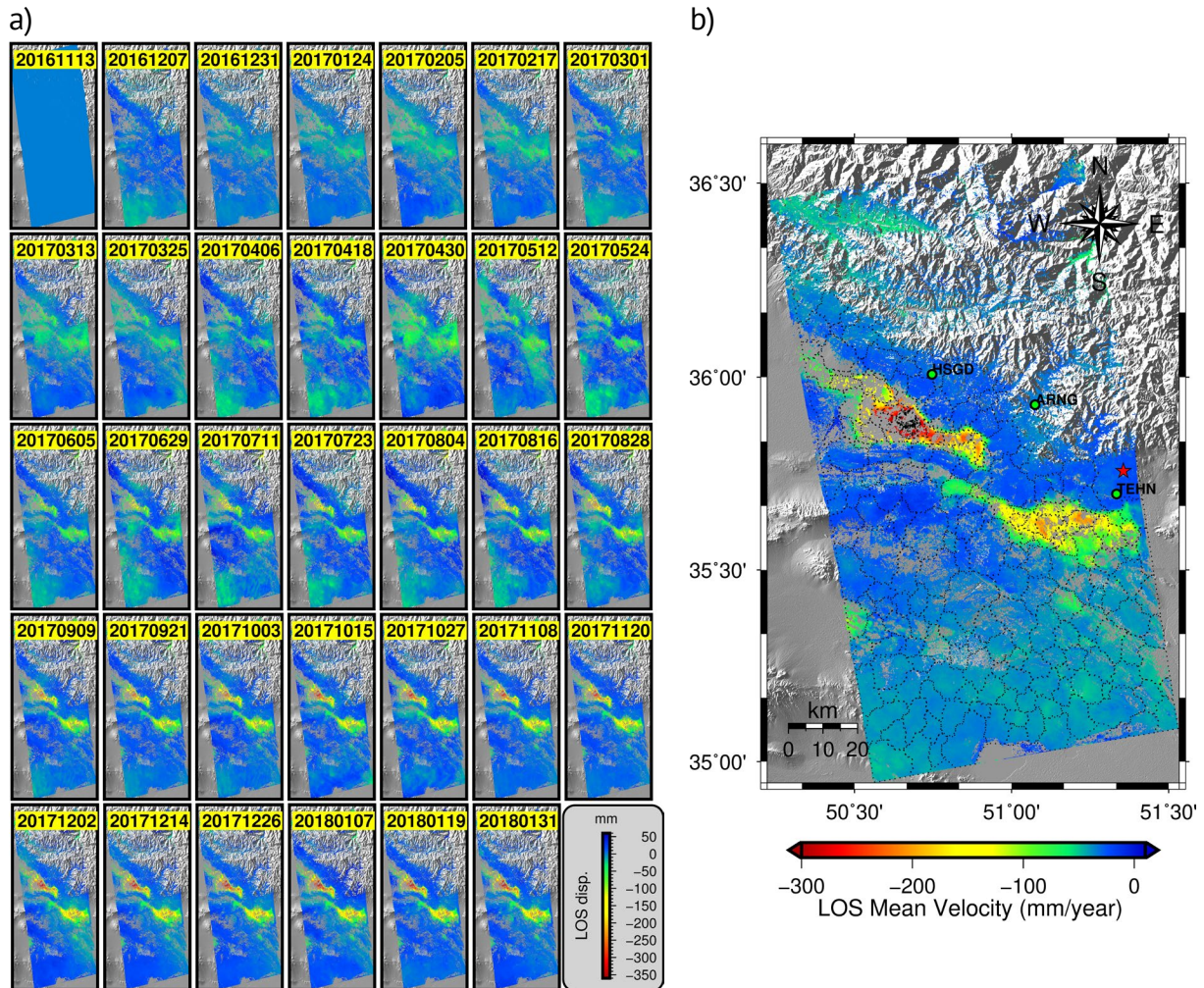


Figure 5. a) The accumulative displacement map is estimated using SBAS timeseries analysis for ascending track of Sentinel-1A SAR images. b) The average LOS velocity map and green dots indicated GPS stations. A polygon with black dash lines represents different classifications on the line of sight velocity map. The red star indicates the location of the reference point used for comparison of the InSAR and GPS datasets.

We used the high redundancy of the interferograms and single-master stacking method to estimate and remove the atmospheric phase delay errors under the atmospheric noise coefficient (ANC) method [Tymofeyeva and Fialko, 2015]. The ANC, quantifying the relative amount of atmospheric noise at each SAR acquisition, enables us to grade the acquisitions, according to the magnitude of the atmospheric contribution, in combination with SBAS timeseries estimation using an iterative approach. Finally, together with ANC correction, we applied a coherence-based SBAS method to compute displacement timeseries and atmospheric corrections for each scene in our region (Figure 5).

Figure 5.b shows the average line of sight (LOS) velocity from the Tehran plain obtained from our analysis. The average LOS velocities map reveals that subsidence has occurred at a high rate in the two regions, the western Tehran and Hashtgerd plains. The maximum observed LOS velocity of the subsiding area is -200 mm/yr and -300 mm/yr in the west of Tehran and Hashtgerd plains, respectively.

After performing the classification described in detail in Section 4, we extracted the PSs within each class. To identify these PSs, the ADI is assumed to be 0.42, and the scene is subdivided into 25 patches with 100 and 400 overlapping pixels in the range and azimuth directions, respectively. After timeseries processing, the total number of stable point candidates or detected PS points were equal to 550,000.

There are several GPS sites in our SAR image frame, however many of them are lacking sufficient temporal overlap with the SAR image timeseries, or their timeseries data is not available to researchers. Thus, three of them, namely, ARNG, HSGD, and TEHN, which contain observations after 2016, are used in this study (Figure 6). However, the ARNG station timeseries was only available until mid-2017.

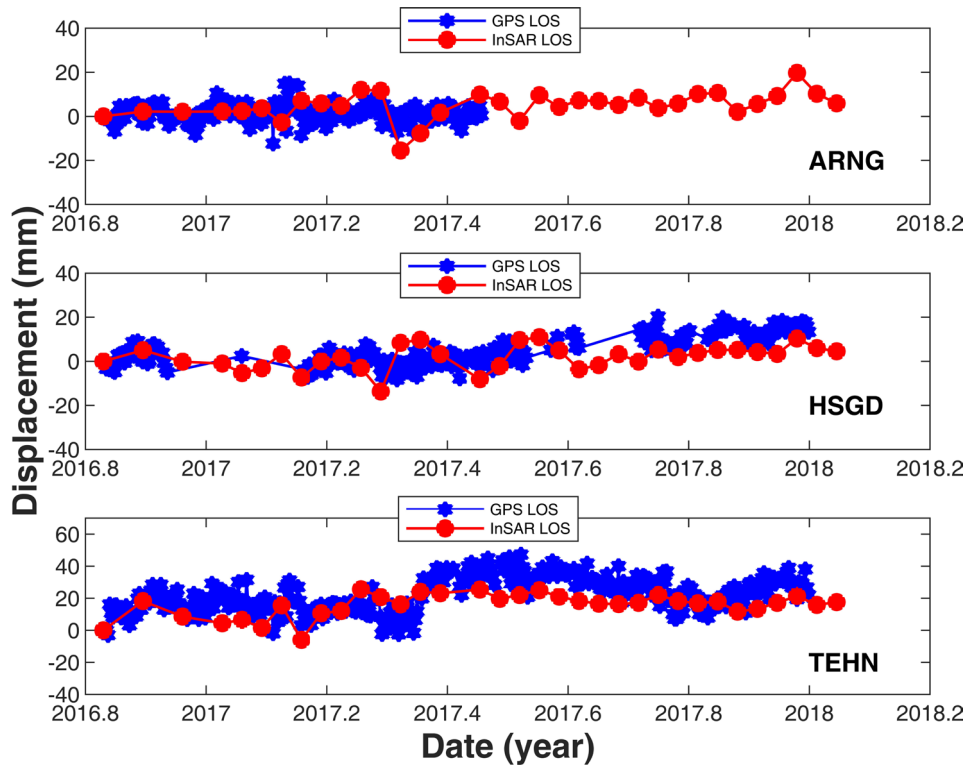


Figure 6. Comparison of GPS and InSAR timeseries derived from Sentinel-1A data at GPS station ARNG (top plot), HSGD (middle plot), and TEHN (down plot). A comparison between InSAR LOS timeseries represented as red dots and GPS-derived LOS timeseries as blue stars.

Our GPS 3D displacement measurements are projected to InSAR LOS direction and then referenced to the equal reference date as InSAR timeseries to compare results. This comparison indicates that the timeseries of permanent GPS stations show good agreement with the InSAR timeseries between 2016 and 2018 (see Table 6). This comparison makes sure that the derived cumulated deformation is valid and effective in the subsequent analysis.

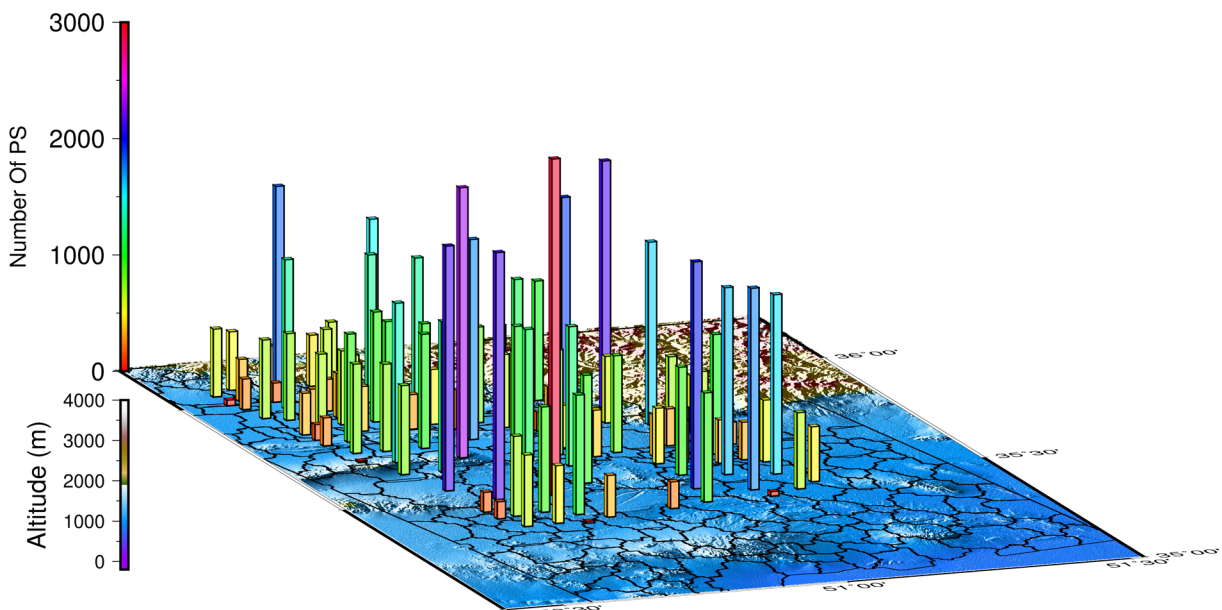


Figure 7. The bars are heightened and coloured based on the number of PS points in each segmentation. The background shows the region’s digital elevation model (SRTM 90).

5.1 Mean Velocity Map Segmentation

To implement the LS-VCE based on the multivariate model, we used a geographical or spatial classification of the final displacement rate map (see Figure 5.b). The reasons for using this type of classification are as follows: 1 – PSs located in a nearby region have similar noise structures, in particular, their atmospheric noise structure, 2 – Our dataset is too large, and there is no separate noise structure defined for each pixel. To applied the proposed approach, we chose a cropped area, i.e., two subsidence fields located away from mountainous areas in the north rather than the full sub-swath because of the following two reasons: (i) to focus on the main AOI, the subsiding areas located in southern Tehran, which has been extensively affected by water-extraction-induced subsidence [Sharifi et al., 2008; Haghighi and Motagh, 2019], (ii) to reduce further the time-consuming computational process (as discussed in Subsection 4.1). As a result, the total number of classes exploited in this area is equal to 370 classes. According to Figure 7, the average number of PSs within each class is about 1000 PSs.

6. Results and Discussion

6.1 LS-VCE per class

As mentioned in section 3, we used the multivariate LS-VCE method to obtain the proper noise structure of the PSs timeseries in a spatial correlation class. The kinematic model (explaining the temporal deformation behaviour), usually used in many TInSAR analyses, is a simple linear model (e.g., Berardino et al. [2002]; Hooper et al. [2004]). According to previous studies proving the existence of periodic behaviours due to seasonal changes and soil dynamic properties [Schenk 2006; Haghighi and Motagh 2019], in addition to the linear behaviour, we add the annual and semi-annual periodic component to the model to accounts for the periodic and seasonal deformations signals as

$$E(\underline{y}) = y_0 + vt + \sum_{k=1}^2 (a_k \cos(w_k t) + b_k \sin(w_k t)) \quad (13)$$

Where t is expressed in terms of a year, and the unknown vector consists of the intercept y_0 , the slope v , and the coefficients a_k and b_k due to annual and semi-annual signals. Also, w_k is the corresponding to the frequency of the sinusoidal signals.

After applying the multivariate LS-VCE method, the functional model was subtracted before noise analysis (removing linear trend, annual, and semi-annual periodic signals). These operations are known as the creation of a “signal-free area”. Then the residual signals that degraded the assumed functional model (such as residual tropospheric error, APS error, orbital error, and temporal decorrelation, or even unmodeled displacement) are known as noise.

To form the stochastic part of the mathematical model as mentioned in subsection 4.2, we tested the combination of different noise structures in a multivariate model using the MLE method and calculated the maximum logarithm of the likelihood function of the stochastic model for each combination (see Table 2).

Noise Model		White + Flicker	White + Autoregressive	Autoregressive + Flicker
Classes	Class1	96.35	124.71	325.97
	Class2	225.81	248.27	439.88
	Class3	87.67	57.65	103.35
	Class4	106.81	136.72	340.88

Table 2. The estimated values of the logarithm of the likelihood function for the different noise structures in the four example classes are shown in Figure 9.

Ultimately the most suitable noise structure is selected in terms of flicker noise plus autoregressive noise. Therefore, the structure of the covariance matrix is close to $D(\text{vec}(\underline{Y})) = \Sigma \otimes Q$ with $Q_y = Q(\sigma_a^2, \sigma_f^2) = \sigma_a^2 Q_a + \sigma_f^2 Q_f$. In each class, as mentioned before, \underline{Y} consists of the timeseries observations of the PSs (e.g., r timeseries). The iterative algorithm of Fig. 1 is now used to estimate both σ_a and σ_f , which represent the temporal noise amplitude of the timeseries. Table 3 gives the estimated temporal noise amplitudes of the example classes introduced in Table 2 for different stochastic models. This Table also provides the precision (σ_θ^2) of the estimates as one of the important features of LS-VCE.

Classes		Class1	Class2	Class3	Class4
Noise Model	White Noise	Negative	Negative	0.47 ±0.07	Negative
	Flicker Noise	6.72 ±1.38	8.82 ±1.71	1.79 ±0.79	5.45 ±2.35
	White Noise	0.28 ±0.01	0.09 ±0.01	0.83 ±0.01	0.39 ±0.02
	Autoregressive Noise	1.19 ±0.05	1.56 ±0.06	0.27 ±0.03	0.98 ±0.08
	Autoregressive Noise	0.02 ±0.01	0.04 ±0.01	0.03 ±0.01	0.02 ±0.01
	Flicker Noise	1.66 ±0.03	1.62 ±0.03	1.77 ±0.03	1.68 ±0.05

Table 3. White noise, flicker noise, and autoregressive noise amplitude estimates as well as their precision (mm²) for the four example classes in three different stochastic models (white noise plus flicker noise; white noise plus autoregressive noise; and flicker noise plus autoregressive noise).

In the following, the multivariate LS-VCE method was implemented in different classes to extract the estimated parameters and their precision for the PS points. Calculating the correlation coefficient between the timeseries of different PSs in each class (Eq. (9) and (10)), we showed this correlation is very high at close intervals and gradually decreases as the interval between the different PS increases. The reason for this correlation can be due to the existence of some spatial correlation components of the phase interferograms (e.g., atmospheric and orbital noise), unmodeled displacement, and even the effects of applying spatial filters. For example, the estimated correlation coefficients and standard deviation given in Tables 4 and 5 obtained for the class around the GPS stations of TEHN and HSGD include a limited number of PS points inside this class.

As mentioned earlier, the stochastic part of the model can be as a $mr \times mr$ covariance matrix of the form

$$D \left(\underbrace{\begin{Bmatrix} y_1 \\ y_2 \\ \vdots \\ y_r \end{Bmatrix}}_{mr \times 1} \right) = \underbrace{\begin{bmatrix} \sigma_1^2 Q & \sigma_{12} Q & \cdots & \sigma_{1r} Q \\ \sigma_{12} Q & \sigma_2^2 Q & \cdots & \sigma_{2r} Q \\ \vdots & \vdots & \ddots & \vdots \\ \sigma_{1r} Q & \sigma_{2r} Q & \cdots & \sigma_r^2 Q \end{bmatrix}}_{mr \times mr} = \Sigma \otimes Q \quad (14)$$

From the estimated matrix Σ , one can also obtain the spatial correlation between different timeseries. This symmetric covariance matrix contains $r(r+1)/2$ covariance components divided into r variances and $r(r-1)/2$ covariances.

$$\Sigma = \begin{bmatrix} \sigma_1^2 & \sigma_{12} & \cdots & \sigma_{1r} \\ \sigma_{12} & \sigma_2^2 & \cdots & \sigma_{2r} \\ \vdots & \vdots & \ddots & \vdots \\ \sigma_{1r} & \sigma_{2r} & \cdots & \sigma_r^2 \end{bmatrix} \quad (15)$$

Figure 9 presents the diagrams of these components against the distance between their corresponding PSs for several classes. These results show that for the PSs adjacent to each other (short arcs), the covariance components between them are high and gradually decrease by increasing distance. We can also observe that the mean

PS code	Distance (m)	Estimated Corr. Coef (%)	Estimated STD (mm)
PS _{TEHN}	0.00	100 ±00.00	10.19 ±0.24
PS1	136.33	99.94 ±5.60E-08	10.81 ±0.26
PS2	202.13	99.16 ±9.95E-06	08.29 ±0.19
PS3	279.21	99.91 ±1.25E-07	10.74 ±0.25
PS4	322.27	99.86 ±2.75E-07	09.98 ±0.24
PS5	392.91	99.49 ±3.65E-06	09.75 ±0.23
PS6	511.11	99.16 ±9.92E-06	09.07 ±0.21
PS7	511.25	99.39 ±5.33E-06	10.48 ±0.27
PS8	524.47	99.52 ±3.22E-06	09.91 ±0.23
PS9	577.73	98.84 ±1.89E-05	09.02 ±0.21
PS10	588.30	99.28 ±7.31E-06	10.30 ±0.24
PS11	678.79	98.36 ±3.76E-05	08.84 ±0.21
PS12	727.22	97.91 ±6.13E-05	08.73 ±0.21
PS13	1861.29	76.03 ±0.006361	12.03 ±0.28

Table 4. Estimated spatial correlations (sorted by baseline length between PSs), standard deviation, and their precision between PS timeseries for a few PSs around the GPS station of TEHN.

PS code	Distance (m)	Estimated Corr. Coef (%)	Estimated STD (mm)
PS _{HSGD}	0	100 ±00.00	07.55 ±9.05E-02
PS1	879.12	97.68 ±7.51E-05	08.05 ±9.65E-02
PS2	1465.05	97.04 ±1.22E-04	07.22 ±8.65E-02
PS3	1865.50	94.35 ±0.00043	07.58 ±0.09082
PS4	2087.57	93.44 ±5.75E-04	07.89 ±9.47E-02
PS5	2329.14	93.30 ±5.99E-04	07.88 ±9.44E-02
PS6	3103.74	87.38 ±2.00E-03	07.92 ±9.50E-02
PS7	3263.64	90.57 ±1.15E-03	07.92 ±9.50E-02
PS8	4023.77	93.78 ±5.19E-04	07.81 ±0.093654
PS9	4277.04	93.84 ±5.09E-04	07.59 ±9.10E-02
PS10	4485.46	71.74 ±8.41E-03	06.90 ±8.27E-02
PS11	5869.61	91.99 ±8.45E-04	07.21 ±8.65E-02
PS12	7789.24	86.40 ±2.30E-03	06.62 ±7.93E-02
PS13	8115.15	85.81 ±2.48E-03	06.71 ±8.05E-02

Table 5. Estimated spatial correlations, standard deviation, and their precision between PS timeseries for a few PSs around the GPS station of HSGD.

variations of the covariance components with respect to the distance between classes are similar to the Gaussian auto-covariance function as visualized in Figure 8 and is given by

$$C_{Gaus}(PS_i, PS_j) = C_0 \exp\left(-\frac{r_{ij}^2}{d^2}\right) \quad (16)$$

where, C_0 , d and r_{ij} are variance, correlation distance, and distance between PS_i and PS_j , respectively. In fact, such an auto-covariance function describes the smooth spatial stochastic process; its smoothness is defined by the correlation distance d and variance component C_0 .

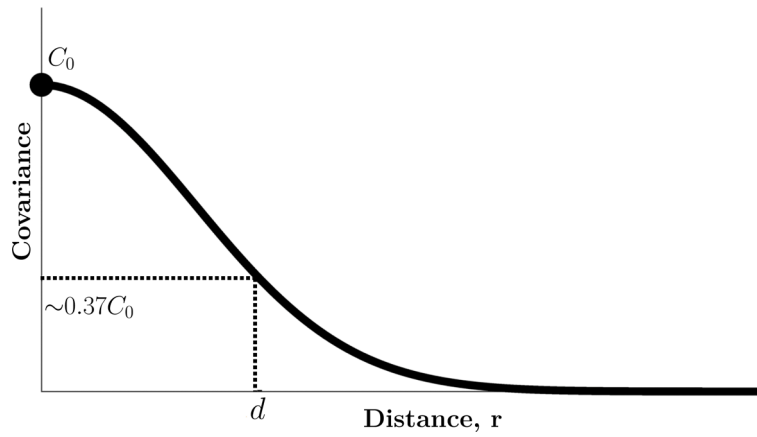


Figure 8. Gaussian auto-covariance function.

Such behaviour in InSAR results is expected as we know that InSAR products are contaminated with spatially correlated noise such as the tropospheric turbulent phase effects or its residuals after atmospheric filtering steps [Hanssen 2001; González and Fernandez 2011].

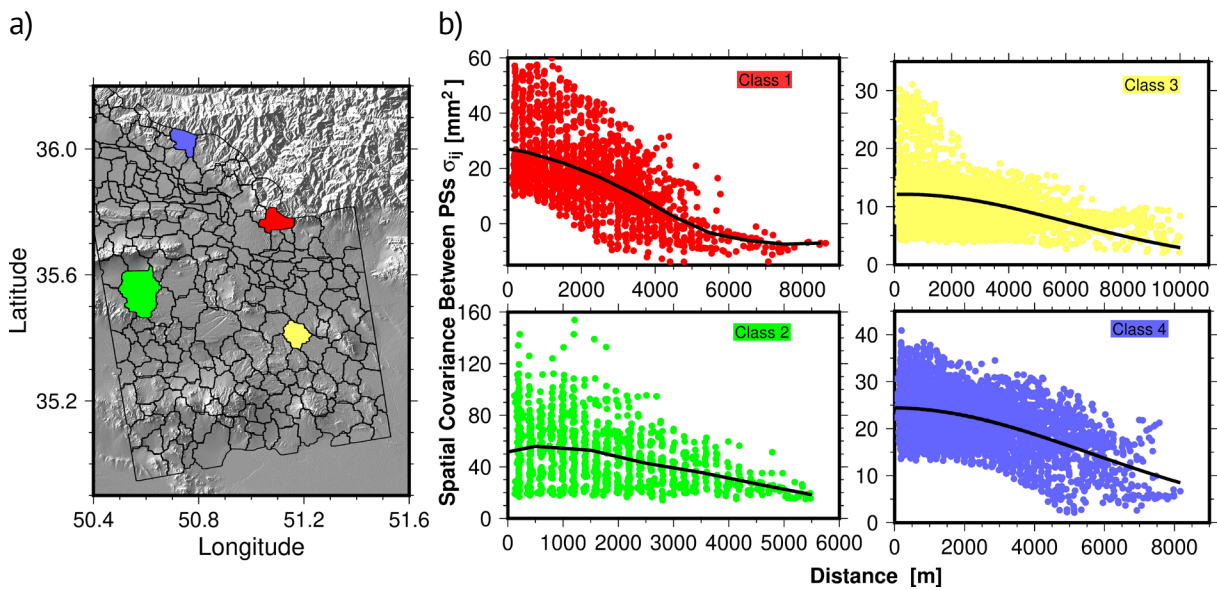


Figure 9. a) The boundary of geographical classes plotted on the topography of the area (SRTM 90). b) Variations of covariance components in the classes marked with different colours relative to the distance between PSs within each class. The black solid curve on each plot indicates the Gaussian function fitted to the data.

Note that we have not used explicit spatial noise models in the initial stochastic modelling (Eq. (2)). Given the fact that the noise structure is similar to the Gaussian auto-covariance function, it would be possible to estimate only the unknown parameters of this function (C_0 , d) instead of computing $r(r-1)/2$ off-diagonal spatial covariance components. Furthermore, according to Eq. (12), one may later add the correlation between the timeseries to the estimated parameters' covariance matrix (i.e., after solving with the univariate model).

6.2 Validation and comparison with GPS data

To validate our results, we used the GPS observations in our case study area. This comparison was initially performed for the three GPS timeseries and then carried out to further evaluate other GPS stations whose only displacement rate was available (Figures 10 and 11). In the first stage, after calculating the appropriate weights of measurements through the multivariate LS-VCE method, The RMSE of InSAR timeseries (weighted and non-weighted) compared with GPS timeseries. Also, to match GPS and InSAR timeseries to one common time period, we used spline interpolation.

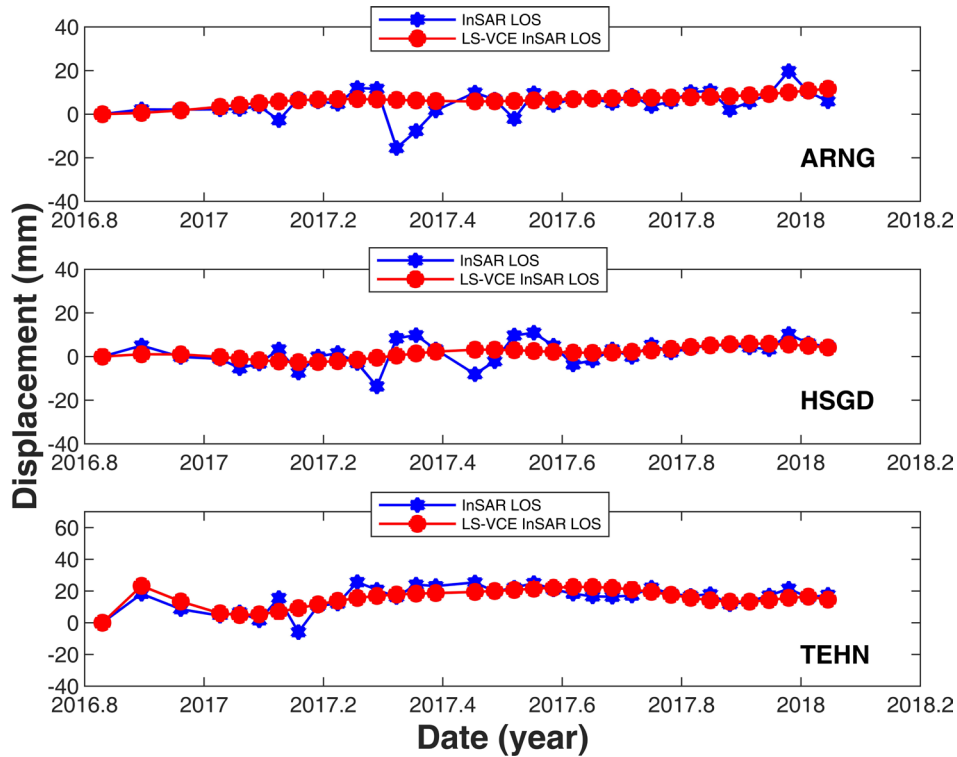


Figure 10. Three timeseries of LOS displacements are shown in Fig. 6: The original InSAR timeseries (blue stars and lines) and corrected timeseries using our approach (red circles and lines).

To quantify our methodology's performance, we compute the RMSE of InSAR timeseries (before and after applying proper weight) relative to GPS timeseries measurements (Table 6).

In the second stage, we compared two different InSAR-derived velocities (one estimated from original data without accounting for the noise structure and the other accounting for the proposed noise structure derived from LS-VCE) with the estimated velocities from GPS sites. The vertical site velocities of the GPS stations are obtained from the study of Raeesi and colleagues [2017]. To get vertical velocities from InSAR data, we have projected InSAR LOS velocities into vertical by dividing them into the local incidence angles (ignoring the horizontal velocities, according to the study of Haghighi and Motagh [2019] for this area). As mentioned earlier, to perform this comparison, the data are compared to each other relative to the reference point shown in Figure 5.b with a red star, which is very close to one of the GPS stations.

GPS Stations	RMSE (mm)	
	Original InSAR	LS-VCE InSAR
ARNG	10.18	5.71
HSGD	12.40	9.90
TEHN	7.89	3.89

Table 6. RMSE between GPS timeseries and InSAR timeseries before and after applying multivariate LS-VCE for three stations is shown in Figure 6.

Subsequently, we have compared the GPS and InSAR vertical velocities by calculating the difference between them. The average RMSE of the misfits of original InSAR and LS-VCE vertical velocities against the GPS vertical velocities is equal to 12.31 and 6.51, respectively (see Table 7). The results show that applying the multivariate LS-VCE method improves the results by about 50% compared with the case where the noise parameters are not considered.

GPS Sites	GPS Velocity (mm/yr)	Original InSAR Velocity (mm/yr)	LS-VCE InSAR Velocity (mm/yr)	Absolute values of	
				Original difference	LS-VCE difference
TEHN	10.86	20.29	7.09	9.43	3.77
HSGD	11.34	1.06	9.91	10.28	1.43
MF13	11.45	4.59	14.01	6.86	2.56
FOPM	11.69	6.87	10.04	4.82	1.65
MF17	10.81	7.09	11.13	3.72	0.32
TN01	13.12	-2.44	4.37	15.56	8.75
FOIM	13.18	-22.31	-13.94	35.49	27.12

Table 7. Comparison between original InSAR velocities and our proposed method.

Furthermore, we can calculate the precision of the model parameters by Eq. (10). In this way, the diagonal elements of the matrix $Q_{\hat{x}}$ indicate the precision of the estimated model parameters. Table 8 shows the precision of the model parameters in the case of estimating the proper noise structure (LS-VCE InSAR) and without considering Original InSAR for a PS near the TEHN station. As shown in Table 8, it is optimistic about calculating the model parameters' precision if the appropriate noise structure is not estimated.

Model parameters (TEHN Station)	The precision of model parameters	
	LS-VCE InSAR	Original InSAR
y_0 (mm)	1.772	0.930
v (mm/yr)	0.849	0.557
a_k {annual} (mm)	0.3468	0.269
b_k {annual} (mm)	0.343	0.256
a_k {semiannual} (mm)	0.251	0.240
b_k {semiannual} (mm)	0.266	0.255

Table 8. Comparison of the precision of model parameters for a PS near the TEHN station.

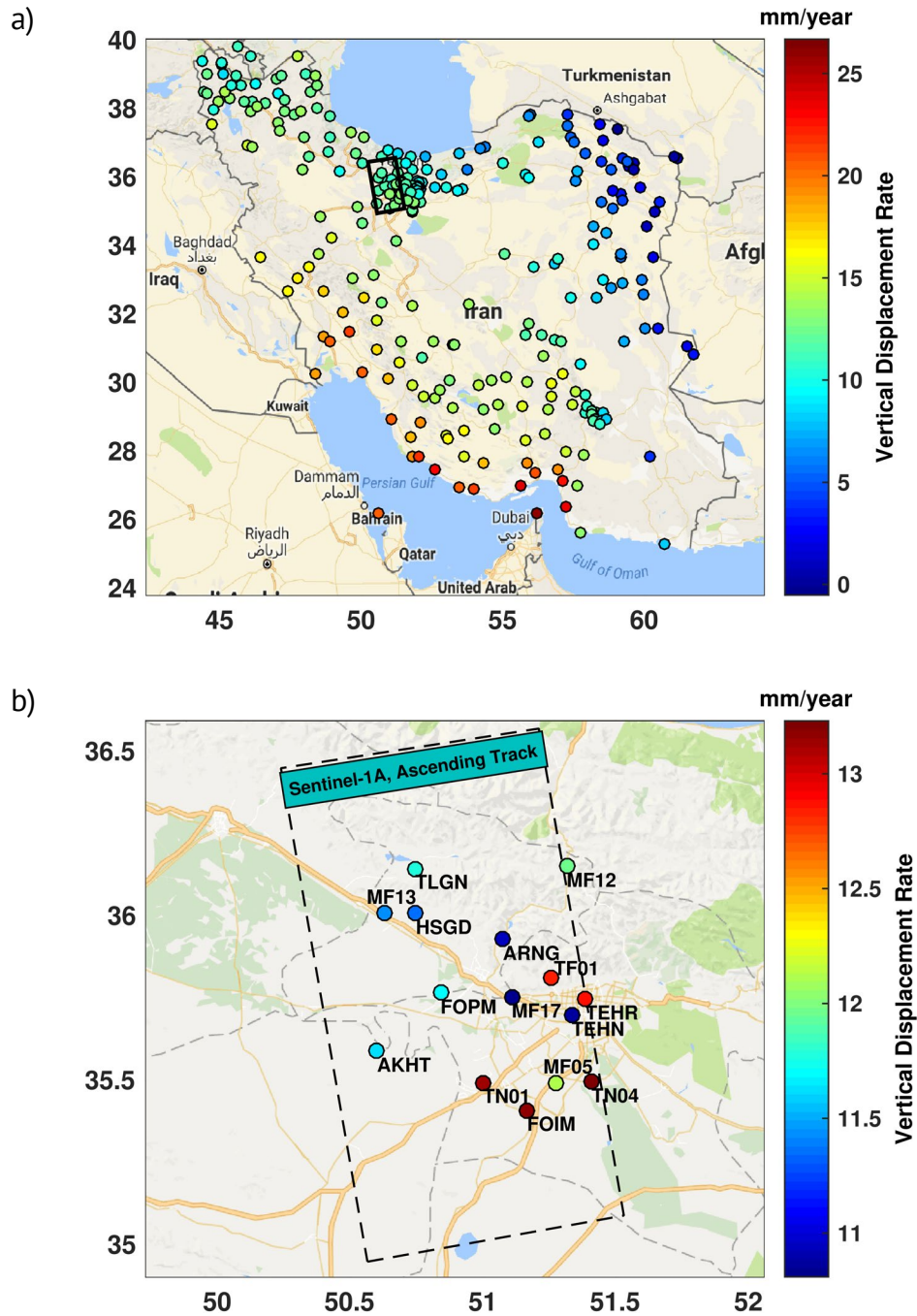


Figure 11. a) GPS stations and GPS vertical velocity field in Iran [Raeesi et al. 2017], small black dash rectangular indicates our processing Sentinel data track, b) Our study area and its GPS stations.

7. Conclusion

This paper proposes estimating the precision and noise structure of the final InSAR-derived deformation timeseries based on the multivariate LS-VCE methodology. We analysed the noise content of the timeseries and presented the precision of the estimated parameters. Our analysis shows that the suitable noise structure for the definition of the stochastic model of observations in our specific case study is a combination of autoregressive and flicker noise models. Applying this combined noise model indicates that there is a high temporal and spatial correlation in the results. In particular, we show that Gaussian covariance functions can model the spatial correlation of the data. We conclude that the spatial noise correlations have a direct influence on the calculation of the estimated parameters. Using the GPS results as the criterion for validation of estimated deformation model param-

eters shows that applying the multivariate LS-VCE method compared with the case where the noise parameters are not considered improves the results by about 50%. We should emphasize that the noise components' structure may differ from one case study to another; but, the proposed methodology is generic. Since the entries of the cofactor matrix are essential for the performance of the multivariate LS-VCE method, it is important that these cofactors are selected correctly according to the case study and the operating algorithm. So, this remains as future work for additional studies and supplementary investigation on other noise models to see how the different noise models may affect the estimated parameters and their precision.

Acknowledgments. We want to thank the European Space Agency that provides open access to the Sentinel-1A SAR data (<https://scihub.copernicus.eu>). Radar processing has been performed in this paper using two software packages, StaMPS (<https://homepages.see.leeds.ac.uk/~earahoo/stamps/>) and GMTSAR (topex.ucsd.edu/gmtsar/). We also thank Dr. Xiaopeng for providing GMTSAR2StaMPS scripts (<http://doi.org/10.5281/zenodo.3387231>) that were used in this paper to convert and preparation data to StaMPS. Most of the figures were drawn using Generic Mapping Tools (GMT5) software (Wessel and Smith 1995). Dr. Behzad Behnabian is acknowledged for proofreading the English of the manuscript.

References

- Adam, N., B. Kampes and M. Eineder (2003). The development of a scientific permanent scatterer system, paper presented at ISPRS Hannover Workshop, Inst. for Photogramm. And Geoinf., Hannover, Germany.
- Agram, P. and M. Simons (2015). A noise model for InSAR time series, *J. Geophys. Res.: Solid Earth*, 120, 4, 2752-2771, <https://doi.org/10.1002/2014JB011271>.
- Amiri-Simkooei, A.R. (2007). Least-squares variance component estimation: theory and GPS applications, PhDthesis, Delft University of Technology, Netherlands.
- Amiri-Simkooei, A.R. (2009). Noise in multivariate GPS position time-series, *J. Geod.*, 83, 2, 175-187, <https://doi.org/10.1007/s00190-008-0251-8>.
- Amiri-Simkooei, A.R., C. Tiberius and S. P. Teunissen (2007). Assessment of noise in GPS coordinate time series: methodology and results, *J. Geophys. Res.: Solid Earth*, 112(B7), <https://doi.org/10.1029/2006JB004913>.
- Baatz, M., U. Benz, S. Dehghani, M. Heynen, A. Höltje, P. Hofmann, I. Lingenfelder, M. Mimler, M. Sohlbach, M. Weber and G. Willhauck (2004). eCognition professional user guide 4, Definiens Imaging, Munich.
- Berardino, P., G. Fornaro, A. Fusco, D. Galluzzo, R. Lanari, E. Sansosti and S. Usai (2001). A new approach for analyzing the temporal evolution of Earth surface deformations based on the combination of DIFSAR interferograms, *Geoscience and Remote Sensing Symposium, IGARSS'01. IEEE International*, <https://doi.org/10.1109/IGARSS.2001.978085>.
- Bert, M. K. (2006). *Radar Interferometry: Persistent Scatterers Technique*, The Netherlands: Springer, <https://doi.org/10.1007/978-1-4020-4723-7>.
- Bui, L. K. (2021). Small baseline subset InSAR data processing: design of interferogram networks and noise analysis in InSAR-derived deformation time series, Curtin University, <http://hdl.handle.net/20.500.11937/83668>.
- Cao, Y., Z. Li, J. Wei, J. Hu, M. Duan and G. Feng (2018). Stochastic modeling for time series InSAR: with emphasis on atmospheric effects, *J. Geod.*, 92, 2, 185-204, <https://doi.org/10.1007/s00190-017-1055-5>.
- Costantini, M., S. Falco, F. Malvarosa, F. Minati and F. Trillo (2009). Method of persistent scatterer pairs (PSP) and high resolution SAR interferometry, *IEEE International Geoscience and Remote Sensing Symposium*, <https://doi.org/10.1109/IGARSS.2009.5417918>.
- Dainty, J. C. (2013). *Laser speckle and related phenomena*, Springer science & business Media, <https://doi.org/10.1007/978-3-662-43205-1>.
- Davenport, W. B. and W. L. Root (1958). *An introduction to the theory of random signals and noise*, McGraw-Hill New York, <https://doi.org/10.1109/9780470544143>.
- Farzaneh, S., M.A. Sharifi, K. Parvazi and B. Namazi (2020). Assessment of noise in time series analysis for Buoy tide observations, *Int. J. Maritime Tech.*, 13, 41-49, <http://ijmt.ir/article-1-688-en.html>.
- Ferretti, A., C. Prati and F. Rocca (2001). Permanent scatterers in SAR interferometry, *IEEE Trans. Geosci. Remote Sens.*, 39, 1, 8-20, <https://doi.org/10.1109/36.898661>.

- González, P. J. and J. Fernandez (2011). Error estimation in multitemporal InSAR deformation time series, with application to Lanzarote, Canary Islands, *J. Geophys. Res.: Solid Earth*, 116(B10), <https://doi.org/10.1029/2011JB008412>.
- Guarnieri, A. M. and S. Tebaldini (2007). Hybrid Cramér–Rao bounds for crustal displacement field estimators in SAR interferometry, *IEEE Signal Proc. Lett.*, 14, 12, 1012-1015, <https://doi.org/10.1109/LSP.2007.904705>.
- Haghighi, M. H. and M. Motagh (2019). Ground surface response to continuous compaction of aquifer system in Tehran, Iran: Results from a long-term multi-sensor InSAR analysis, *Remote Sens. Environ.*, 221, 534-550, <https://doi.org/10.1016/j.rse.2018.11.003>.
- Hanssen, R. F. (2001). Radar interferometry: data interpretation and error analysis, Springer Science & Business Media, <https://doi.org/10.1007/0-306-47633-9>.
- Hooper, A., H. Zebker, P. Segall and B. Kampes (2004). A new method for measuring deformation on volcanoes and other natural terrains using InSAR persistent scatterers, *Geophys. Res. Lett.*, 31, 23, <https://doi.org/10.1029/2004GL021737>.
- Hooper, A. and H. A. Zebker (2007). Phase unwrapping in three dimensions with application to InSAR time series, *JOSA A*, 24, 9, 2737-2747, <https://doi.org/10.1364/JOSAA.24.002737>.
- Hooper, A. J. (2006). Persistent scatter radar interferometry for crustal deformation studies and modeling of volcanic deformation, Stanford University.
- Ketelaar, V. G. (2009). Satellite radar interferometry: Subsidence monitoring techniques, Springer Science & Business Media.
- Lanari, R., P. Lundgren, M. Manzo and F. Casu (2004). Satellite radar interferometry time series analysis of surface deformation for Los Angeles, California, *Geophys. Research Lett.*, 31, 23, <https://doi.org/10.1029/2004GL021294>.
- Lucido, M., F. Meglio, V. Pascazio and G. Schirinzi (2009). Closed-form evaluation of the second-order statistical distribution of the interferometric phases in dual-baseline SAR systems, *IEEE Trans, Signal Proc.*, 58, 3, 1698-1707, <https://doi.org/10.1109/TSP.2009.2037849>.
- Mehrabi, H., B. Voosoghi, M. Motagh and R.F. Hanssen (2019). Three-dimensional displacement fields from InSAR through Tikhonov regularization and least-squares variance component estimation, *J. Surv. Engineer.*, 145, 4, 04019011, [https://doi.org/10.1061/\(ASCE\)SU.1943-5428.0000289](https://doi.org/10.1061/(ASCE)SU.1943-5428.0000289).
- Raeesi, M., Z. Zarifi, F. Nilfouroushan, S.A. Boroujeni and K. Tiampo (2017). Quantitative analysis of seismicity in Iran, *Pure Appl. Geophys.*, 174, 3, 793-833, <https://doi.org/10.1007/s00024-016-1435-4>.
- Samiei-Esfahany, S. and R. Hanssen (2017). On the evaluation of second order phase statistics in SAR interferogram stacks, *Earth Obs. Geomatics Engin.*, 1, 1, 1-15, <https://doi.org/10.22059/EOGE.2017.63865.1016>.
- Samiei Esfahany, S. (2017). Exploitation of distributed scatterers in synthetic aperture radar interferometry, PhDthesis, Delft University of Technology, Netherlands, <https://doi.org/10.4233/uuid:22d46f1e-9061-46b0-9726-760c41404b6f>.
- Sandwell, D., R. Mellors, X. Tong, M. Wei and P. Wessel (2011). Gmtsar: An insar processing system based on generic mapping tools.
- Sandwell, D. T. and E. J. Price (1998). Phase gradient approach to stacking interferograms, *J. Geophys. Res.: Solid Earth*, 103(B12), 30183-30204, <https://doi.org/10.1029/1998JB900008>.
- Schenk, A. (2006). Interpreting surface displacement in Tehran/Iran region observed by differential synthetic aperture radar interferometry (DINSAR), PhDthesis, MSc thesis, Tech. University, Berlin, Germany.
- Sharifi, M., M. Motagh, S. Aipour, V. Akbari, T. Walter, M. Rajabi, F. Samadzadegan, Y. Djamour and M. Sedighi (2008). InSAR time-series analysis of land subsidence due to groundwater overexploitation in groundwater basins of central and northeast Iran, *AGU Fall Meeting Abstracts*, G31B-0661.
- Strozzi, T., U. Wegmuller, L. Tosi, G. Bitelli and V. Spreckels (2001). Land subsidence monitoring with differential SAR interferometry, *Photogram. Engineer. Remote Sens.*, 67, 11, 1261-1270.
- Sudhaus, H. and J. Sigurjón (2009). Improved source modelling through combined use of InSAR and GPS under consideration of correlated data errors: application to the June 2000 Kleifarvatn earthquake, Iceland, *Geophys. J. Int.*, 176, 2, 389-404, <https://doi.org/10.1111/j.1365-246X.2008.03989.x>.
- Teunissen, P. J. and A. Amiri-Simkooei (2008). Least-squares variance component estimation, *J. Geod.*, 82, 2, 65-82, <https://doi.org/10.1007/s00190-007-0157-x>.
- Tymofyeyeva, E. and Y. Fialko (2015). Mitigation of atmospheric phase delays in InSAR data, with application to the eastern California shear zone, *J. Geophys. Res.: Solid Earth*, 120, 8, 5952-5963, <https://doi.org/10.1002/2015JB011886>.

- Van der Kooij, M. (2003). Coherent target analysis, Proceedings of the third International Workshop on ERS SAR Interferometry (FRINGE 2003), Frascati (Italy).
- Van der Ziel, A. (1979). Flicker noise in electronic devices, *Adv. Electron. El. Phys.*, Elsevier, 49, 225-297, [https://doi.org/10.1016/S0065-2539\(08\)60768-4](https://doi.org/10.1016/S0065-2539(08)60768-4).
- Van Leijen, F. J. (2014). Persistent scatterer interferometry based on geodetic estimation theory.
- Wessel, P. and W. H. Smith (1995). New version of the generic mapping tools, *Eos, Trans. Am. Geophys. Union*, 76, 33, 329-329, <https://doi.org/10.1029/95EO00198>.
- Williams, S.D., Y. Bock, P. Fang, P. Jamason, R.M. Nikolaidis, L. Prawirodirdjo, M. Miller and D.J. Johnson (2004). Error analysis of continuous GPS position time series, *J. Geophys. Res.: Solid Earth*, 109(B3), <https://doi.org/10.1029/2003JB002741>.
- Zhang, J., Y. Bock, H. Johnson, P. Fang, S. Williams, J. Genrich, S. Wdowinski and J. Behr (1997). Southern California Permanent GPS Geodetic Array: Error analysis of daily position estimates and site velocities, *J. Geophys. Res.: Solid Earth*, 102(B8), 18035-18055, <https://doi.org/10.1029/97JB01380>.

***CORRESPONDING AUTHOR: Masoud MASHHADI HOSSAINALI,**

Department of Geodesy and Geomatics Engineering, K. N. Toosi University of Technology, Tehran, Iran,
email: hossainali@kntu.ac.ir (M.M. Hossainali).